

A Convex Phased Array Ultrasonic Inspection Gauge for Small-Diameter Pipelines with Enhanced Resolution and Sensitivity

Christian Peyton, Dayi Zhang, *Senior Member, IEEE*, Mehrab Zamanian, Nick Bettley, Hugh Lewis, Ehsan Mohseni, David Lines, and Gordon Dobie

Abstract—Accurate measurement of wall thickness and defect detection is essential for pipeline integrity. Small-diameter pipelines (4-6 inches), common in distribution networks, flowlines, and process systems, are difficult to inspect because they are often buried, insulated, or otherwise inaccessible. Ultrasonic pipeline inspection gauges (PIGs) provide a solution, but to navigate the tight bends found in traditional “unpiggable lines” a short form factor unibody PIG is required. Conventional unibody PIGs rely on multiple carriages and large transducer elements that achieve high signal-to-noise ratio (SNR) with fewer channels at the expense of spatial resolution. Conversely, reducing element size increases resolution but also raises the inactive fraction of the aperture, weakening signals and reducing beam uniformity. To address these limitations, this paper presents a proof-of-concept inspection instrument based on a convex phased array with small elements. Compensation is applied through coherent transmit sub-apertures and multi-element receive beamforming. Simulations using Huygens modelling show that a 128-element convex array achieves full circumferential coverage in 4-6” pipes. Importantly, the 128-element design provides approximately four times the resolution of a 32-element array while maintaining comparable SNR, thereby overcoming the traditional trade-off. Two industrial-focused experiments confirmed the benefits of compensation. In the 4” pipe, compensation achieved an SNR improvement of 15.34 dB compared with uncompensated operation, along with a reduction in wall-thickness measurement error by 0.59 mm and in measurement uncertainty by 1.43 mm. In the 6” pipe, tests further demonstrated reliable detection of 2 mm flat-bottom holes, which equivalent to 0.8% of the pipe’s circumference. Together, these findings demonstrate that phased-array compensation overcomes the traditional trade-off between resolution and sensitivity, enabling compact ultrasonic PIG tools to inspect 4-6” pipelines with high reliability.

Index Terms—Pipeline inspection gauge, Convex ultrasonic array transducers, Inline inspection, Non-destructive testing, Small-diameter pipelines

I. INTRODUCTION

ENSURING the structural integrity of pipelines is critical to preventing failures and maintaining safe operation. Pipelines transport oil, gas, and chemicals across long distances, and failures caused by corrosion, wall thinning, or

Manuscript created February 11, 2026; This research was funded by Innovate UK Knowledge Transfer Partnerships (KTP13391) in collaboration with Cobeusters Ltd. (Chester, UK).

Christian Peyton and Nick Bettley are with Cobeusters Ltd., The Armoury Building, Hawarden Aviation Park, Flint Road, Chester CH4 0GZ, U.K. (email: cpeyton@cobeusters.com)

Christian Peyton, Dayi Zhang, Mehrab Zamanian, Ehsan Mohseni, David Lines, and Gordon Dobie are with the Department of Electronic and Electrical Engineering, University of Strathclyde, Royal College Building, 204 George Street, Glasgow, G1 1XW, U.K. (e-mail: dayi.zhang@strath.ac.uk).

Hugh Lewis is with Square Wave Technology. (email: hugh@squarewave.co.uk)

cracking can lead to major safety, environmental, and economic consequences. Accurate and quantitative measurement of wall thickness therefore plays a central role in assessing pipeline condition and guiding maintenance decisions [1], [2].

A wide range of non-destructive testing (NDT) methods are applied to pipelines, including magnetic flux leakage, eddy current, and ultrasonic techniques [3], [4]. Each of these methods is effective for certain defect types, but none provides complete coverage across all possible damage mechanisms. To address this limitation, hybrid tools that combine multiple NDT technologies are also deployed to improve the detectability of difficult defects [5], [6]. While these approaches can be effective in controlled conditions, many pipelines are buried, insulated, or located in inaccessible environments, which makes external inspection difficult and costly. Additionally, many small-diameter lines were not designed with inspection in mind, complicating access and navigation. Pipelines with diameters between 4 - 6 inches (outer diameters 114.3–168.3 mm) represent a particularly important but challenging case. These small-diameter lines are widely used in distribution networks, flowlines, and process systems, yet their restricted geometry makes them among the most difficult to inspect.

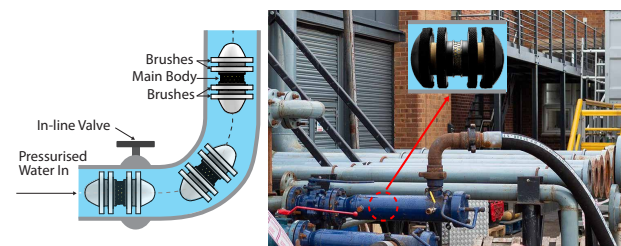


Fig. 1. Principle and example setup for pipeline inspection using a PIG. The PIG is positioned inside the pipe and connected to a valve assembly. A hydraulic hose pump supplies pressurised water to maneuver the PIG through the pipeline.

The integration of advanced NDT technologies into compact inline inspection instruments represents a critical step forward—enhancing precision and enabling inspection through challenging geometries such as in-line valves and short-radius bends. These instruments, commonly known as pipeline inspection gauges (PIGs), as Fig. 1, travel inside the pipe and perform long-range assessments of wall condition, corrosion and geometric anomalies without requiring excavation or service interruption. Propelled by the pressure of the transported fluid, the PIG advances under the differential force created across the tool, allowing it to traverse bends, negotiate vertical sections and adapt to changes in orientation. Modern PIGs function as carrier platforms that can

accommodate different sensing payloads depending on the inspection objective; for example, video-based tools capture images of the inner surface, while ultrasonic and magnetic payloads provide quantitative measurements of wall thickness and corrosion. Because the instrument operates entirely within the water-filled steel pipeline, external communication is not possible during inspection, so all sensing, processing, storage and power management must be performed autonomously. This self-contained operating environment imposes strict constraints on the mechanical envelope, power budget and sensor architecture: the onboard battery must sustain the inspection over long distances, the tool must remain compact enough to negotiate short radius bends, valves and welds, and the sensing modules must maintain stable coupling as the PIG continuously moves through the pipe. These practical constraints limit the size and number of sensing elements that can be deployed in small-diameter pipelines and motivate the need for novel transducer architectures, such as the compact convex phased array proposed in this work, that can deliver high resolution and high sensitivity within the restricted physical footprint available.

Recent developments in inline inspection (ILI) of small-diameter pipelines have increasingly focused on overcoming conventional limitations through innovative sensing and smart PIG technologies. Smart PIGs, employing ultrasonic, electromagnetic, and eddy current systems, have been evaluated for their respective capabilities in anomaly detection and defect sizing in steel pipelines. Extending beyond these modalities, broader surveys encompass electromagnetic, acoustic, optical, and robotic systems, while also highlighting persistent challenges such as limited adaptability to complex environments, trade-offs between accuracy and inspection efficiency, and high equipment costs [7], [8]. [9] proposed a inline impedance-based method for leakage detection in nonconducting water mains, capable of locating very small leaks in non-metallic PVC pipes. [10] introduced an electromagnetic coupling inline inspection system using a magnetic ring structure that combines magnetic flux leakage and alternating current field measurement. The method improves adaptability and sensitivity for detecting cracks and corrosion in small-diameter pipelines. [11] introduced a remanent magnetic flux leakage method that improves crack and corrosion detection in pipelines via hysteresis, but its performance is limited by lift-off since sensors float in water. Optical solutions such as [12], [13], [14] offer excellent surface profiling and defect detection, they are limited by the turbidity of the medium. While these literatures demonstrate the breadth of available inspection technologies, they also emphasise that significant limitations remain in achieving reliable, high-resolution inspection of small-diameter pipelines.

Among the available methods, ultrasound is particularly attractive because it provides direct, quantitative volumetric measurements with high spatial resolution and is less affected by variations in material composition compared to electromagnetic techniques. Conventional ultrasonic pipeline inspection gauges are therefore widely used to detect corrosion, wall thinning, and geometric anomalies. These tools employ piezoelectric transducers that transmit and receive ultrasonic

waves through a liquid coupling medium inside the pipeline, as shown in Fig. 2(a)(b). Using the pulse-echo method, a short ultrasonic pulse is launched toward the pipe wall and the echoes returning from material interfaces are recorded. The time interval between the front-wall and back-wall reflections,

$$d = \frac{c_{steel} t_{BW}}{2} \quad (1)$$

, is proportional to the local wall thickness, where d is thickness, c_{steel} is the longitudinal velocity of steel, and t_{BW} is the measured round-trip time-of-flight inside the steel wall between the front-wall and back-wall echoes. Corrosion, erosion, and wall thinning reduce this time-of-flight, while geometric features or internal defects modify the amplitude, shape, or timing of the received echoes [15], [16]. In conventional PIGs, many discrete transducers are distributed around the tool circumference, each producing an A-scan corresponding to one angular position. As the tool advances, these A-scans are combined to form B-scans and thickness maps, allowing the reconstruction of wall-thickness profiles and the identification of defects such as pits, gouges, or laminations.

To ensure pipeline integrity, inspection tools must be sensitive to small defects such as pitting corrosion and localised thinning. Detecting these features requires finer spatial sampling, which in turn demands smaller transducer elements to increase resolution. However, reducing element size lowers the acoustic energy that can be transmitted and received, thereby decreasing the SNR. This trade-off is further compounded by manufacturing constraints: the spacing between adjacent elements (kerf) cannot be reduced below a certain limit, so miniaturisation inevitably increases the number of kerfs, reducing the effective active aperture area, transmitted power, and SNR. While SNR can in principle be improved by increasing excitation power or using coded excitation techniques, both approaches are challenging in practice—higher power is limited by the small batteries available in compact PIGs, and coded excitation is difficult to implement in dynamic, fast-moving inspection environments [17]. Geometric constraints add another layer of complexity: in small-diameter pipelines, the limited pitch circle diameter (PCD) restricts transducer placement and causes coverage gaps [8]. These gaps are often mitigated by adding offset axial rows, but this increases tool length and complexity, reducing manoeuvrability through bends and valves. In larger pipes, the opposite issue arises, as conventional PIGs cannot adapt beam geometry to varying diameters, leading to reduced coverage and SNR.

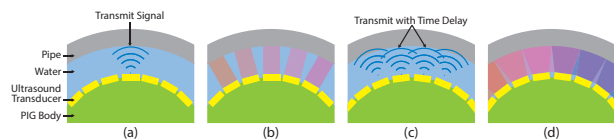


Fig. 2. Schematic illustration of ultrasound transmission methods: (a) a single transducer element transmitting into the pipe wall, (b) single transducer element transmitting in sequence, (c) 4 elements transmitting with time delays, and (d) 4 elements transmitting in sequence.

To address these limitations, phased array ultrasonic testing (PAUT) provides a powerful alternative. Unlike single-element

probes, phased arrays use many individually controlled elements to steer and focus the beam (Fig. 2(c)(d)), enabling circumferential coverage across varying pipe diameters and greater sensitivity to localised defects [18]. By applying programmed time delays, the emitted wavefronts constructively focus at a chosen location, allowing electronic steering and focusing without mechanical movement. Advanced approaches such as full matrix capture and the total focusing method [19] further improve resolution and defect sensitivity, broadening PAUT's use in medical imaging, aerospace, and pipeline inspection [18], [19].

Building on these principles, several studies have explored the use of PAUT for pipeline inspections [20], [21], [22], where compact geometries make conventional UT impractical. The application of PAUT in pipeline inspection has demonstrated significant potential to overcome the coverage limitations of conventional ultrasonic tools. Curved and flexible PAUT probes have been developed to achieve full circumferential coverage in small-diameter tubes, enabling the detection of corrosion and cracks in geometries where rigid probes are impractical [23]. Industrial examples include dedicated curved array scanners capable of achieving 360° coverage in pipes as small as 21 mm in diameter [24]. While these approaches illustrate the versatility of PAUT for constrained environments, they also highlight key limitations: reduced steering range in short-radius convex arrays, potential beam distortion near the array's near field, and the increased electronic complexity required for dense element configurations [18]. Thus, while promising, existing PAUT implementations remain constrained in their applicability to inline inspection of 4–6 inch pipelines.

Although PAUT is well established, most studies use external transducers. In pipelines, the probe cannot be repositioned, so mid-line failures both end the inspection and obstruct the pipe. To fit the bore while covering the wall, probes adopt a compact convex array, where elements lie on a curve rather than a plane [25]. Delay laws are needed to focus the beam, and high element density prevents grating lobes and poor contrast. Beam coverage can be improved with sub-aperture stepping. [26] designed a 256-element circular PAUT PIG for natural gas pipelines, optimised via simulations of aperture, frequency, and spacing. However, the work remains at the simulation stage without experimental validation.

Despite progress in ultrasonic inline inspection, existing discrete-element ultrasonic PIGs for 4–6 inch pipelines remain constrained by the trade-off between resolution and sensitivity. Large transducer elements provide strong signals and high SNR but sacrifice spatial resolution, whereas smaller elements improve resolution at the cost of weaker signals and reduced effective aperture due to fixed inter-element spacing. These limitations motivate the development of a compact convex phased-array solution that combines finer elements with array compensation to achieve both reliable defect sensitivity and full circumferential coverage in small-diameter pipelines.

To address these limitations, this paper presents a proof-of-concept convex phased-array ultrasonic PIG for 4–6 inch pipelines, designed to overcome the trade-off between spatial resolution and sensitivity that limits existing small-diameter inspection tools. The proposed approach combines finer el-

ements with phased-array compensation to achieve complete circumferential coverage, reliable wall-thickness measurement, and enhanced detection of defects as small as 2 mm, while remaining compact enough to navigate pipelines down to 4 inches in diameter.

The main contributions of this paper are:

- A compact 128-element convex phased-array architecture is developed for internal ultrasonic inspection of 4"–6" pipelines.
- A curvature-compensated sub-aperture beamforming method is formulated for phased arrays operating on cylindrical geometries.
- A geometric design framework is established that relates array pitch, curvature, and beamwidth to the achievement of complete circumferential coverage.
- An internally deployable implementation of the convex phased array within a 56 mm inline inspection tool is demonstrated under realistic operating constraints.

The paper is organised as follows. Section II describes the convex array configuration and the operating principles of the 128-element phased-array system. Section III describes the Huygens-based simulation of the array beam profile. Section IV reports the experimental validation of the prototype instrument, including comparisons against a 32-element PIG. Section V summarises the conclusions and future work.

II. CONVEX ARRAY CONFIGURATION AND SYSTEM OPERATING PRINCIPLE

A. Practical Design and Operational Constraints

The design was governed by several practical constraints inherent to inline inspection. Inline tools are generally limited to about 50% of the nominal bore, as larger instruments are prone to sticking in 1.5D elbows and valves. Accordingly, the body diameter was constrained to 56 mm, preserving at least 20 mm of radial clearance to accommodate weld beads, ovality, and internal deposits, thereby ensuring safe navigation. The transducer length was set at 6 mm, enabling reliable passage through short-radius bends and reduced-bore valves while still allowing space for transducer elements, electronics, and fluid coupling. A minimum kerf of 0.15 mm was enforced, reflecting fabrication limits associated with the convex array geometry.

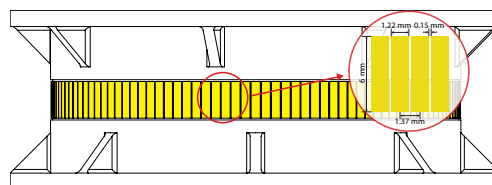


Fig. 3. Schematic of the convex phased-array layout showing the transducer element arrangement around the PIG body. The individual array elements with a width of 1.22 mm, kerf spacing of 0.15 mm, and an active element height of 6 mm, forming a circumferential aperture length of 1.37 mm.

Operational constraints were also considered. The tool travel speed was set in the range of 0.2 to 0.8 m/s to balance stability, coupling, and data quality: the lower bound ensures

sufficient flushing flow and reliable coupling, while the upper bound avoids turbulence, excessive data throughput, and drag forces that hinder navigation through tight bends. Within these boundaries, the array was designed with 1.22×6 mm elements to maximise circumferential resolution (perpendicular to the PIG travel axis), as shown in Fig. 3. The central frequency of the ultrasonic transducer was 5 MHz.

B. Convex Array Geometry and Element Distribution

The sensing module employs a 128-element convex phased array arranged uniformly around a pitch-circle diameter of 56 mm (radius 28 mm), forming a complete circumferential ring. The total available arc length on this circle is therefore

$$L_{circ} = 2\pi R = 2\pi \times 28 \text{ mm} = 175.93 \text{ mm} \quad (2)$$

With 128 equally spaced elements, the resulting circumferential pitch is

$$p = \frac{L_{circ}}{128} = 1.37 \text{ mm} \quad (3)$$

which defines the maximum arc length allocated to each element position. A manufacturing kerf (k) of 0.15 mm is required between neighbouring elements to maintain electrical and mechanical isolation. Subtracting this kerf from the circumferential pitch yields an active element width of

$$w = p - k = 1.22 \text{ mm} \quad (4)$$

Although the circumferential pitch could, in principle, be reduced by increasing the number of elements on the pitch circle, several practical limitations restrict how far this can be taken. Each element requires a kerf for electrical and mechanical isolation, and as the element count increases, the kerf occupies a progressively larger fraction of the pitch. In the present 128-element design, the active-to-pitch ratio (w/p) is approximately 89%. Increasing the count to 256 would reduce the pitch to 0.53 mm but lower w/p to around 78%, making the kerf a significant portion of the available aperture and reducing the effective radiating area. Further increases also impose tighter constraints on matching-layer fabrication, cabling density and backing design, and substantially increase the data volume that must be acquired and processed during inline inspection. These combined acoustic and system-level considerations place a practical upper bound on the number of usable elements in small-diameter convex arrays and motivate selecting a configuration that balances sampling resolution with manufacturability and overall instrument complexity.

C. Geometric Constraints on Beamforming and Local Aperture Selection

In the proposed design, the 128 elements are distributed uniformly around a 56-mm pitch-circle diameter, forming a convex circumferential array in which each element is oriented along its own radial direction toward the pipe wall. Because these radial orientations differ around the circle, elements separated by larger angular distances insonify different regions of the wall and do not share a common propagation path. As a result, a full-aperture 128-element transmit law cannot produce meaningful constructive interference; only neighbouring

elements, whose radial pointing vectors are nearly aligned, can contribute coherently to the same insonified region. This geometric constraint fundamentally limits the size of any usable coherent aperture on a circumferential convex array.

For this reason, a four-element local transmit aperture is used. Four adjacent elements provide sufficient effective aperture to improve sensitivity through coherent summation, while remaining small enough that their propagation directions are compatible with the pipe geometry. Larger coherent groups would also span angles where the propagation paths diverge, reducing beam coherence and introducing distortion. This grouping also simplifies switching and timing control, which is essential for compact inline inspection hardware. These geometric considerations define the allowable coherent aperture size.

D. Sub-Aperture Stepping Scheme and 360° Circumferential Coverage

To obtain full circumferential coverage of the pipe wall, the 4-element local sub-aperture is electronically stepped through all 128 element positions on the pitch circle. Each element is individually addressable, allowing the sub-aperture to be advanced by one element at a time without any mechanical motion.

For each measurement, a contiguous group of 4 adjacent elements is activated coherently to generate a local radial beam directed toward the nearest region of the inner pipe wall. As illustrated in Fig. 4(a) and (b), the sub-aperture then advances by one element at a time - from elements i to $i + 3$ in Fig. 4(a) to elements $i + 1$ to $i + 4$ in Fig. 4(b).

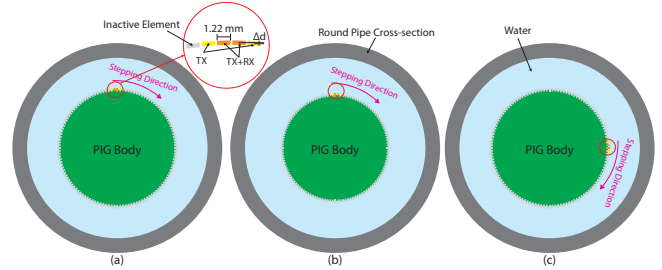


Fig. 4. Illustration of the electronically stepped 4-element sub-aperture around the 128-element circumferential array. Orange indicates the central transmit TX and receive RX element, yellow the transmit TX-only elements with advance ($-\Delta t$), and grey the inactive elements. (a) Initial sub-aperture (i to $i + 3$). (b) One-element shift ($i + 1$ to $i + 4$). (c) After 32 steps. Stepping through all 128 positions at 2.81° increments provides full 360° coverage at the 1.37-mm pitch.

Repeating this procedure across all indices produces 128 sequential sub-apertures, each corresponding to a distinct circumferential position. This electronic stepping samples the full 360° circumference at the intrinsic 1.37-mm pitch, equivalent to an angular increment of $\Delta\theta = 360^\circ/128 = 2.81^\circ$. At each stepped position, the corresponding echo signals are acquired, with each sub-aperture contributing one circumferential sample at the element pitch. Because neighbouring apertures overlap spatially, the resulting data set provides continuous and uniformly spaced coverage around the pipe wall. The combination of the fine sampling interval and the

reduced beam footprint of the 4-element sub-aperture yields a significantly denser circumferential spatial resolution than that achievable with traditional single-element PIG probes.

This stepping strategy therefore provides complete 360° insonification of the pipe interior while preserving the geometric and beamforming constraints imposed by the convex array architecture.

E. Beamforming Formulation and Rationale for Water-Path Delay Compensation

Conventional phased-array focusing laws assume a flat, stationary aperture in which all elements share a common insonification direction and a fixed stand-off distance. In a circumferential convex array mounted on an inline inspection tool, neither assumption holds. The elements are distributed around a cylindrical body, each with a different radial orientation, so only neighbouring elements insonify the same region of the pipe wall; applying a full-aperture focal law would therefore misalign the transmitted wavefronts rather than reinforce them. Moreover, the PIG does not remain perfectly centred but floats within the pipe, causing the stand-off to vary during operation and further disrupting the phase relationships required for conventional focusing. For these reasons, only local delay compensation is applied. Small water-path differences between adjacent elements are equalised so that a 4-element sub-aperture behaves as an effectively flat array. This minimal phase alignment enables coherent addition without full steering or focusing and avoids the hardware and computational burden associated with conventional focal laws, which is essential for compact inline inspection hardware.

Therefore, the present system adopts a water-path-based delay scheme derived directly from the physical height differences between adjacent element centres. Let the additional propagation distance between element i and its neighbour $i-1$ be Δd , as shown in Fig. 4; the corresponding incremental delay is

$$\Delta t = \frac{\Delta d}{c} \quad (5)$$

, where $\Delta d = d_i - d_{i-1}$ is the additional water path length between the centre of element and the centre of its neighbour element, and c is the sound velocity in water (1483 mm/s). For this 128-element design, the additional path length of 0.067 mm corresponds to a delay of 45 ns.

The resulting transmit field can be written in standard delay-and-sum form. Let $u(t)$ denote the excitation pulse and w_n the aperture weights. The four-element transmit signal is

$$s_{TX}(t) = \sum_{n=1}^4 w_n u(t - t_{n,TX}) \quad (6)$$

In the present device, no apodisation or adaptive optimisation is applied, so uniform weighting is used: $w_n = 1, n = 1, \dots, 4$.

On receive, only the two central elements of each sub-aperture are combined, so using a simple delay-and-sum formulation. If $r_n(t)$ denotes the ultrasound signal received at element n , the receive beamformed signal is

$$s_{RX}(t) = \sum_{n \in 2,3} v_n r_n(t) \quad (7)$$

, with unity weights $v_2 = v_3 = 1$ and zero receive delay.

This avoids the need for receive-side delay compensation across the curved aperture and substantially reduces the data volume and processing load, which is critical for inline inspection tools with constrained onboard computing and memory resources.

The resulting water-path-based delay strategy therefore provides a coherent, low-complexity beamforming method that respects the geometric constraints of the convex array and remains compatible with the limitations of an inline inspection platform

III. SIMULATION OF CONVEX ARRAY BEAMFORMING PERFORMANCE

A. Simulation Setup

Simulation played a central role in assessing phased-array beamforming performance, providing insights into beam behaviour and coverage that would be difficult or costly to obtain experimentally. Huygens modelling [27], [28], implemented in MATLAB, was employed to benchmark small-element arrays against a 32-element, 6 mm-diameter reference PIG with an identical body and to evaluate the effect of applying delay laws in a convex geometry. This approach enabled direct comparison of uncompensated and compensated arrays, clarifying how phased-array compensation can recover signal amplitude and improve spatial resolution for pipeline inspection. All simulation results were normalised to the 6 mm reference PIG. This ensures that comparisons between small elements, the uncompensated array, and the compensated array are made relative to a fixed sensitivity baseline, highlighting the extent to which phased-array compensation can recover signal strength while also improving resolution.

To ensure adequate numerical accuracy, each 1.22×6 mm element was discretised into point sources with a spatial interval of 0.01 mm, providing more than 1/20 of the acoustic wavelength sampling at the operating frequency of 5 MHz. The acoustic field was calculated on a two-dimensional domain of 20 mm in the lateral direction and 200 mm in the axial direction, sampled at 0.1 mm. This window spans the entire water path between the convex array face and the inner pipe wall for both 4'' and 6'' geometries. The model assumes an unbounded medium with no interfaces present. All key parameters used in Huygen's modelling are summarised in Table I.

The propagation medium was modelled as water with a longitudinal velocity of 1483 m/s, representing the flooded environment of inline inspection tools and providing a homogeneous coupling layer for the comparison of beam behaviour. Only the water region was explicitly simulated; the steel pipe wall was treated as the distal boundary of the computational grid without modelling reflection or transmission coefficients. This simplification isolates the influence of element width, spacing, curvature and delay laws on beam formation. A full water-steel-water model would introduce additional effects,

TABLE I
HUYGENS SIMULATION PARAMETERS

Category	Parameter	Value / Description
Element discretisation	Point-source spacing	0.01 mm
	Element size	1.22×6 mm
Computational grid	Lateral span	20 mm
	Axial span	200 mm
	Grid resolution	0.1 mm
Acoustic medium (water)	Longitudinal velocity	1483 m/s
Physics assumptions	Propagation model	Linear, homogeneous
	Pipe wall	Treated as distal boundary (no reflection modelling)
Frequency	Operating frequency	5 MHz

such as mode conversion and surface roughness, which influence absolute echo amplitude but do not affect the relative coherence and divergence comparisons central to this study.

Based on Huygens' principle, every point on a wavefront can be treated as a source of secondary wavelets; the resulting wavefront is obtained by summing their contributions. In this approach, an ultrasonic wavefront is represented as a series of point sources, each generating spherical (or circular in 2D) wavelets. The far-field amplitude of each source is given by

$$P(r) = A \frac{1}{\sqrt{r}} e^{i(kr - \omega t)} \quad (8)$$

where P is the power, A is a complex number representing the sources amplitude and phased, r is the distance travelled, k is the wavenumber, ω is the angular frequency and t is time. Summing the contributions of all point sources within each array element produces the overall beam profile. The model represented a circumferential-radial slice of the convex array, which is appropriate because the 6 mm element height is uniform and significantly larger than the circumferential pitch. Summing the contributions of all point sources yielded the complete beam map for each transmit configuration. The model was used to investigate the effect of element number, element width and curvature radius on array behaviour under both uncompensated and delay-compensated operation.

B. Simulation Results

The simulated beam maps are presented in Fig. 5, while the corresponding beam profiles extracted along the pipe wall are shown in Fig. 6. The basis for evaluating the beam maps is threefold. First, the main-lobe intensity and uniformity provide a measure of the transmitted signal strength, which directly governs echo detectability. Second, the focusing behaviour on the 4'' and 6'' pipe walls, visible as distinct concentrated regions of high amplitude, shows how effectively the aperture steers energy toward the inspection surface. Third, the magnitude and distribution of side lobes relative to the main lobe indicate the extent of off-axis insonification, with lower side-lobe levels corresponding to improved contrast, reduced artefacts and better circumferential resolution during inspection. Together, these criteria form the basis for comparing array configurations and assessing the effectiveness of the applied delay laws.

The 6 mm single-element PIG was modelled as the reference case to benchmark amplitude and beam quality. As shown in the Fig. 5(a), the aperture produces a highly directional field, but the distance to the 4'' pipe wall places the observation point inside the transducer near field. For a 6 mm aperture at 5 MHz in water, the near-field is approximately 30 mm, while the water path between the element face and the pipe wall is 24 mm (given the 28 mm transducer offset within the 56 mm tool body and a 52 mm pipe radius). Therefore, the beam profile in Fig. 6(a) shows a reduced on-axis amplitude at 0°, a consequence of partial cancellation between contributions from the transducer edges and centre. Slightly off-axis, constructive interference restores amplitude, giving the profile its characteristic dip-and-rise shape. This behaviour illustrates that, although the 6 mm element provides strong overall amplitude, its interaction with the convex geometry and near-field structure limits beam uniformity. Nevertheless, this case defines the performance ceiling against which smaller elements and phased-array compensation are evaluated.

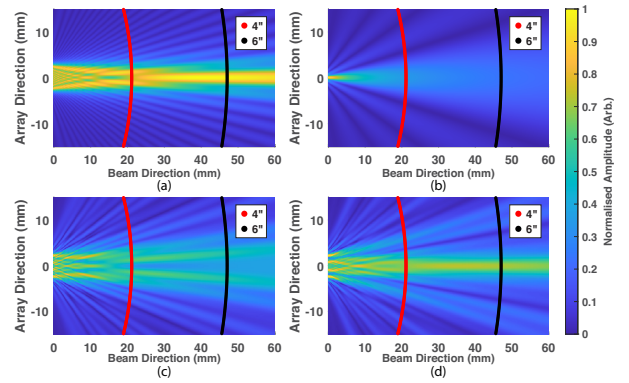


Fig. 5. Beam maps for: (a) a 6 mm single transducer element, (b) a 1.22 mm single transducer element, (c) an array of four 1.22 mm transducer elements without delay rule compensation, and (d) an array of four 1.22 mm transducer elements with delay rule compensation. All amplitudes are normalised to the maximum amplitude obtained by the 6 mm element on a 4'' pipe. The red curves indicate the inner diameter position of the 4'' pipe, while the black curves indicate that of the 6'' pipe.

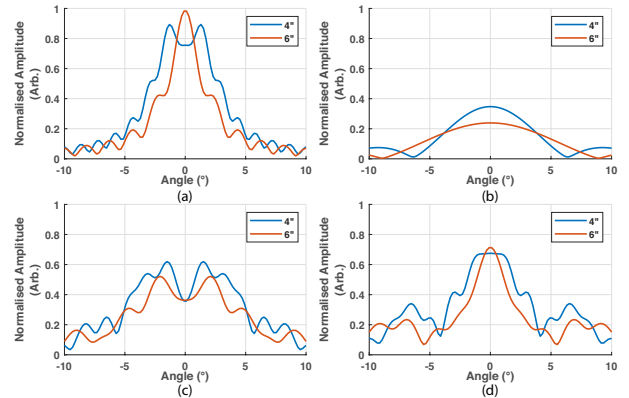


Fig. 6. Beam profiles of (a) a 6 mm single transducer element, (b) a 1.22 mm single transducer element, (c) an array of four 1.22 mm transducer elements without delay rule compensation, and (d) an array of four 1.22 mm transducer elements with delay rule compensation. The amplitudes are normalised to the maximum amplitude in the 6 mm element beam map (Fig. 5(a)).

When the aperture was reduced to a single 1.22 mm element, the beam behaviour changed markedly compared with the 6 mm reference. The beam map in Fig. 3(b) shows a broad, divergent field with rapid spreading before reaching the pipe wall, consistent with the much shorter near-field length. Fig. 4(b) exhibits a substantially lower peak amplitude (less than 25% of the 6 mm reference) and a wide main lobe with elevated pedestal energy. These results confirm that although finer elements increase circumferential sampling density, they do so at the expense of acoustic energy delivery, highlighting the resolution / sensitivity trade-off that motivates phased-array compensation.

The performance of multiple small elements was next assessed by simulating a four-element array without delay laws. As shown in Fig. 5(c), the combined output lacks coherence, resulting in a fragmented acoustic field with multiple lobes and interference fringes. The corresponding wall profile in Fig. 6(c) contains irregular peaks and no dominant main lobe, indicating that the geometric aperture increase alone does not translate into useful energy concentration. Peak amplitude remains lower than the 6 mm reference, demonstrating that four elements without the delay rule not only fail to recover sensitivity but also degrade beam quality compared with a single small element. This establishes the necessity of phase alignment if arrays of fine elements are to function as an effective PIG.

Introducing delay laws based on water-path differences between element centres can significantly improve the response. With compensation applied, the 4-element array generated a coherent, directional beam Fig. 5(d), with constructive addition along the intended axis and visibly reduced side lobes. At the wall, the profile in Fig. 6(d) exhibited a sharpened main lobe and amplitude recovery approaching 70–75% of the 6 mm reference. The beam direction plot Fig. 6(d) further confirmed proper phase alignment, with the main lobe centred on the inspection axis and residual side lobes consistent with the element pitch.

The -6 dB beamwidths of the beam profiles as in Fig. 6 provide a measure of the instantaneous acoustic footprint for each aperture. For the 6 mm element, the -6 dB widths were 6.38° and 2.67° on the 4" and 6" pipe walls, respectively. For the compensated four-element (4×1.22 mm) aperture, the corresponding -6 dB widths were 6.93° and 3.56° . These results show that the compensated sub-aperture produces a lateral beamwidth that is comparable to that of the 6 mm reference element across both pipe sizes, indicating that the delay law successfully combines the four small elements into a single coherent effective aperture.

Although the -6 dB beamwidths quantify the instantaneous acoustic footprint of each aperture, they do not determine the circumferential resolution of the overall system. In a circumferential array, the final spatial resolution is governed by the sampling pitch around the pipe rather than the diffraction-limited beamwidth of individual transmit events. The 128-element configuration samples the circumference four times more densely than the 32-element reference PIG; therefore, the overall circumferential spatial resolution improves by a factor of four despite the similar -6 dB beamwidths observed

in Fig. 6.

In summary, the simulation results illustrated a single 1.22 mm element produced a broad, divergent field with low peak amplitude, while an uncompensated four-element array generated incoherent lobes and poor beam quality. In contrast, the compensated array achieved coherent phasing, producing a well-defined main lobe and restoring approximately 70–75% of the peak amplitude of the 6 mm reference PIG. These results confirm convex phased-array beamforming can offset the sensitivity loss inherent in miniaturised elements while simultaneously improving angular resolution, thereby providing a practical solution for high-fidelity inspection of 4–6" pipelines.

IV. PRACTICAL EXPERIMENTAL VALIDATION

A. Experimental Setup

To validate the simulation findings, a prototype 128-element, piezoelectric, convex phased-array PIG was manufactured by an external local partner to the specified geometry. As is standard in industrial PAUT transducers, internal fabrication processes (e.g., piezoelectric machining, matching-layer construction, backing materials) are proprietary and not disclosed. However, all measurable specifications relevant to acoustic performance and scientific reproducibility were verified upon delivery and are summarised in Table II.

The experiments evaluated wall-thickness measurement accuracy, signal-to-noise ratio, and defect-detection capability under realistic inspection conditions. Performance was compared directly with a 32-element reference PIG of identical body dimensions and with 6 mm element diameter, as presented in Fig. 7.



Fig. 7. Main ultrasonic bodies of the PIGs used in the practical experiments: the left device is the 32-element reference, and the right device is the 128-element phased-array. The brushes of the PIGs are not shown, as they would obscure the main ultrasonic body, the primary object of this paper.

To ensure reproducibility, additional details of the transducer configuration, data acquisition, and calibration methodology are provided here. The 128-element convex array and the 32-element reference PIG were driven by a PeakNDT MicroPulse6 system using a -50 V, 100 ns unipolar excitation pulse and 30 dB receiver gain, as Fig. 7. For each transmit event, the 4-element sub-aperture was excited coherently, and only the two central elements were used on receive, consistent with the delay-law strategy described previously. Signals were digitised at 50 MHz sampling frequency, which provides more than eight samples per cycle at 5 MHz and ensures accurate reconstruction of the back-wall echoes. Acquisition was synchronised with the electronic stepping of the array, producing one A-scan per aperture position.

TABLE II
PHYSICAL AND ELECTRICAL SPECIFICATIONS OF THE CONVEX PHASED ARRAY

Parameter	Value	Notes
Number of discrete elements	128	Uniform circumferential distribution
Centre frequency	5 MHz	All elements identical
Element active width	1.22 mm	Circumferential direction
Element active height	6 mm	Axial direction
Kerf	0.15 mm	Manufacturer's minimum isolation requirement
Pitch-circle diameter (PCD)	56 mm	Body constraint of the PIG
Circumferential pitch	1.37 mm	PCD circumference / 128
Coupling medium	Water	Flooded internal pipeline environment

Calibration for wall-thickness measurements was conducted using steel calibration blocks manufactured from the same material as the test pipes. These blocks had precisely machined thicknesses of 8 and 10 mm, ensuring that acoustic velocity, attenuation, and back-wall reflectivity were representative of the actual inspection specimens. The longitudinal wave velocity used for TOF-to-thickness conversion was verified as 5900 m/s by comparing the measured time-of-flight between successive back-wall echoes with precision calliper measurements. The TOF-derived thicknesses agreed with the physical dimensions within ± 0.05 mm, confirming the correctness of the velocity value.

For defect detection, a reflector was classified as detected when its echo amplitude exceeded 3 dB above the local noise floor. This threshold was selected to match common industrial practice while ensuring sensitivity to the smallest (2 mm) flat-bottom holes. These calibration procedures provided a controlled and traceable basis for evaluating SNR, wall-thickness accuracy, and defect-detection performance.

Two steel pipe sections were used to evaluate array performance. A 4-inch sample with a smooth internal bore was selected for evaluations of wall-thickness measurement accuracy and signal-to-noise ratio because this diameter represents the most challenging case for acoustic beam formation and also corresponds to the smallest target inspection pipe size. Using a defect-free section allowed the influence of pipe curvature, clearance, and coupling conditions on the ultrasonic beam to be characterised in isolation, without the added complexity of scattering from artificial reflectors. This ensured any variations in the measured beam profiles could be attributed directly to the PIG itself and delay laws rather than defect geometry.

By contrast, a 6-inch defect test sample was used to investigate defect detection capability. The sample consisted of 24 machined flat-bottom holes (FBHs) on the external wall, each representing 50% wall loss. Five defect diameters were included: 2, 4, 6, 8, and 10 mm. Four replicas of each size were distributed around the circumference, except for the 4 mm diameter, where eight defects were introduced. Each FBH was axially offset from its neighbours to avoid overlap in the ultrasonic response, while also assessing sensitivity variations across the length of the elements. This geometry enabled a

full 360° circumferential inspection while ensuring controlled machining tolerances and reliable positioning of the array.

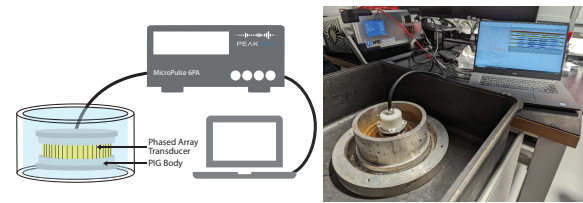


Fig. 8. Practical experimental setup. The prototype ultrasonic phased array in the 6-defect and plugged into the laptop for data capture and Peak NDT MicroPulse6 phased array controller.

As shown in Fig. 8, the PIG body is smaller than the pipe bore, and during the manual experiments the tool was positioned parallel to the pipe in static water, which resulted in a small off-centre positioning. In operational conditions, the tool is equipped with circumferential guide brushes (Fig. 1) mounted at both ends of the PIG, which maintain mechanical alignment and minimise eccentric motion as it travels through the pipe, while still allowing passage through valves and tight-radius bends. The convex phased-array transducer is located at the centre of the PIG body between the two brush assemblies and therefore remains approximately concentric with the pipe wall during inspection. Any remaining offset from the pipe axis does not materially affect the wall-thickness measurement, because thickness is determined from the time difference between successive back-wall echoes, as Eq. 1, rather than from an absolute time-of-flight referenced to the transducer position. Any influence of eccentric positioning is therefore primarily associated with a reduction in SNR under unfavourable tool-pipe geometry and a very slight loss of focus, rather than a systematic error in the measured wall thickness. Furthermore, the overall axial length of the PIG limits the achievable pivot angle within the pipe, reducing the magnitude of angular misalignment during inspection. Additionally, water pressure does not introduce a systematic error in the wall-thickness measurement, since the longitudinal wave velocity in steel is effectively insensitive to hydrostatic pressure over the operating range.

It is worth noting that, although phased-array ultrasonic testing is widely used in external pipeline inspection, the established technology for internal inline inspection in small-diameter pipelines (4''–6'') remains the single-element ultrasound PIG. These represent the commercially deployed state of the art for internal inspection in this diameter range and therefore form the most relevant baseline for evaluating improvements in sensitivity, resolution and circumferential coverage. In contrast, existing phased-array systems are designed for external application and typically employ flat or flexible apertures that must be physically pressed against the outer pipe surface. For example, commercially available flexible PAUT probes [29], [30] are intended for elbows and large-radius pipes and cannot be deployed inside a 4''–6'' pipeline or conform to a 56 mm PIG body. Because external PAUT systems differ fundamentally in geometry, aperture configuration, coupling conditions and mechanical constraints, a direct comparison with such probes would not provide a meaningful

assessment. Consequently, the single-element ultrasound PIG serves as the appropriate industrial benchmark for evaluating the performance of the proposed convex phased-array design.

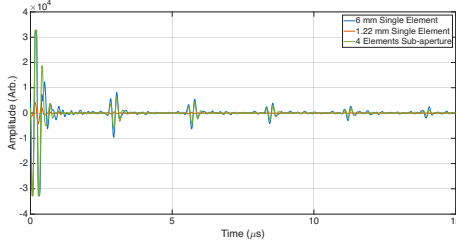


Fig. 9. Ultrasound A-scan signals obtained in the 4'' pipe.

B. 4'' Pipe Experimental Results

Representative A-scan signals obtained in the 4'' pipe are shown in Fig. 9 for three configurations: a single 6 mm element, a single 1.22 mm element, and a four-element 1.22 mm sub-aperture array operated with beamforming delays. The 6 mm single element produces the strongest and cleanest waveform, as expected from its larger active aperture and higher transmitted acoustic energy; the direct arrival, first back-wall reflection, and subsequent multiples are clearly visible with high signal-to-noise ratio. In contrast, the single 1.22 mm element yields a noticeably weaker and noisier echo train, consistent with the reduced aperture size and corresponding drop in transmit power. Applying appropriate delay compensation to the four-element 1.22 mm array substantially improves the signal quality: the combined response recovers a stronger, cleaner A-scan that approaches the clarity of the 6 mm reference while retaining the finer spatial resolution afforded by the smaller elements.

To further quantitatively compare the signal quality across configurations, the signal-to-noise ratio (SNR) was evaluated, as it directly reflects the detectability of echoes and the reliability of subsequent measurements. The SNR was computed using the ratio between the peak amplitude of the first back-wall echo A_{echo} and the amplitude of noise level A_{noise} , in a pre-echo region where no ultrasonic reflections are present. This calculation follows the expression

$$SNR = 20 \log_{10} \left(\frac{A_{echo}}{A_{noise}} \right) \quad (9)$$

The single 6 mm element produced an SNR of 27.23 dB on average, with a 1.89 dB standard deviation (95% confidence interval: 26.84–27.61 dB). The single 1.22 mm element produced a noticeably weaker back-wall echo, yielding an SNR of 13.02 dB on average, with an 8.57 dB standard deviation (95% confidence interval: 11.51–14.53 dB). When four 1.22 mm elements were combined with beamforming delays, the SNR increased to 28.36 dB on average, with a 4.38 dB standard deviation (95% confidence interval: 27.59–29.14 dB). This represents an improvement of 15.34 dB compared with the single 1.22 mm element. Overall, these results show that beamforming successfully recovers the SNR lost in the

miniaturised elements, restoring performance to a level comparable with the 6 mm reference.

Wall thickness was estimated by measuring the time-of-flight between successive back-wall echoes in each A-scan, using an acoustic velocity of 5900 m/s. For each configuration, the echoes from all active elements were analysed, and the mean and standard deviation were computed to provide a measure of accuracy and repeatability. The reference thickness was 8 ± 0.1 mm, measured with callipers.

The single 1.22 mm element measured the wall at 7.44 mm on average, with 1.48 mm standard deviation (95% confidence level: 7.17–7.71 mm), exhibiting a noticeably larger deviation from the true wall thickness as well as greater standard deviations between elements, which can be attributed to its low SNR. In contrast, the compensated four-element array measured 8.03 mm on average, with 0.06 mm standard deviation (95% confidence level: 8.02–8.04 mm), which reduced the absolute error by about 0.59 mm and placed the result well within the ground truth measurement uncertainties. This improvement reflects both greater accuracy relative to the true wall thickness and markedly reduced measurement uncertainty, providing a more reliable measurement than the single element. These results confirm the expected trend that as array coherence improves, both SNR and thickness accuracy increase, and the associated measurement error decreases.

Using the full set of A-scans from each configuration, the corresponding B-scan images were reconstructed to visualise the circumferential wall profile, as Fig. 8. The 6 mm reference PIG (a) provides the strongest, most uniform circumferential response, producing a smooth and well-defined inner wall. The single 1.22 mm element (b) shows weaker amplitudes and increased nonuniformity due to its lower SNR. When the four-element 1.22 mm array are beamformed (c), the image becomes noticeably cleaner and more continuous, recovering much of the clarity of the 6 mm case while retaining the finer spatial resolution of the smaller elements

Overall, the 4'' pipe experiments demonstrate that phased-array mitigates the signal lost in small elements, improving not only the amplitude of the back-wall echo but also the reliability of wall-thickness estimation

C. 6'' Pipe Experimental Results

Unlike the 4'' pipe, the 6'' specimen contained artificial flat-bottom hole defects intended to evaluate defect detectability rather than wall-thickness accuracy. Because the primary objective was to assess whether defects could be reliably identified around the pipe circumference, thickness measurements were not emphasised in this configuration. Therefore, B-scan imaging of defects provides a more meaningful benchmark in the 6'' pipe than thickness estimation, as it is created by collecting A-scan signals and mapping the reflections from the pipe's inner and outer walls along the scanning direction to form a cross-sectional image.

Fig. 11 shows B-scans acquired using the 6 mm reference PIG, a single 1.22 mm element, and a four-element 1.22 mm array with delay laws. The 6 mm reference image exhibits the highest overall signal strength but relatively poor spatial

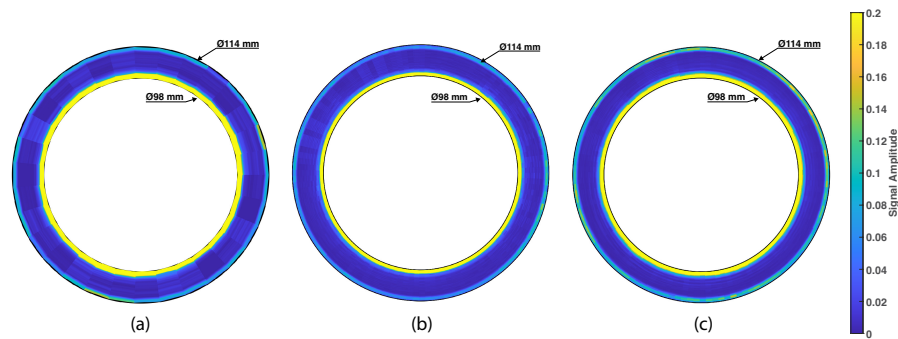


Fig. 10. B-scan imaging of a 4'' pipe section showing reflections from pipe walls, obtained by collecting A-scan signals and mapping them along the scanning direction to generate a cross-sectional view of the pipe wall. Note that the diameters are not to scale, enlarged for better defect visualisation. (a) 6 mm reference PIG, strong overall signal but poor spatial resolution. (b) Single 1.22 mm element, finer spatial resolution but weak amplitudes. (c) Compensated four-element 1.22 mm array, providing both sufficient amplitude and improved resolution.

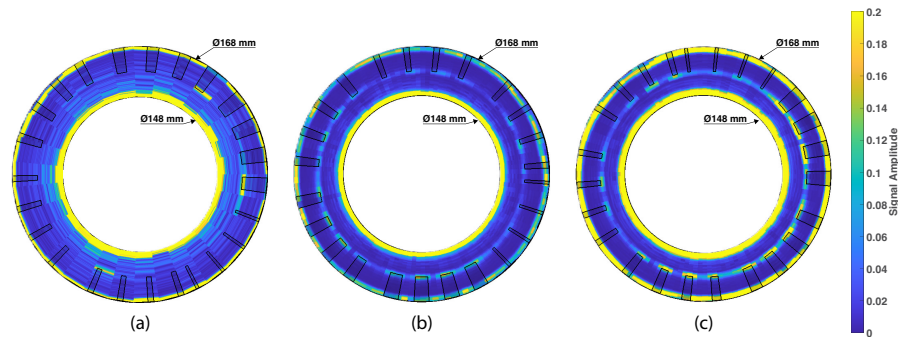


Fig. 11. B-scan imaging of a 6'' pipe section showing reflections from pipe walls and defects, obtained by collecting A-scan signals and mapping them along the scanning direction to generate a cross-sectional view of the pipe wall. The black rectangular boxes indicate the ground-truth locations of machined FBHs. Note that the diameters are not to scale, enlarged for better defect visualisation. (a) 6 mm reference PIG, strong overall signal but poor spatial resolution, making small defects difficult to resolve. (b) Single 1.22 mm element, finer spatial resolution but weak amplitudes, with smaller features often falling below the noise floor. (c) Compensated four-element 1.22 mm array, provides both sufficient amplitude and improved resolution, clearly resolving all defect indications.

resolution, making small defects difficult to resolve against the back-wall response. The single 1.22 mm element should produce a finer lateral resolution and enable more distinct defect indications. However, the corresponding amplitudes are weak, and several smaller features fall below the noise floor. The compensated four-element array provides both sufficient amplitude and improved resolution, providing clearer defect indications across the scan.

Defect detectability was quantified by counting the number of flat-bottom holes that produced identifiable responses exceeding 3 dB above the local noise floor in the B-scan images. The 6 mm reference PIG detected 3 out of 24 defects, primarily the larger ones. The single 1.22 mm element identified 17 defects, showing improved spatial localisation but weaker signals. The compensated array produced the best result, successfully detecting all 24 defects, including the smaller flat-bottom holes whose diameters were 0.8% of the circumference and were missed by the other two configurations. These results demonstrated that phased-array compensation improves both sensitivity and resolution, enabling reliable identification of small defects in larger-diameter pipes.

In summary, the 6'' B-scan experiments highlight the complementary benefits of convex phased-array compensation. While large single elements provide strong signals and small elements provide finer sampling, the compensated array de-

livers both simultaneously, achieving the defect sensitivity required for practical inline inspection.

V. CONCLUSION

In conclusion, this paper has presented the development and validation of a convex phased-array ultrasonic system for inline inspection of 4–6'' pipelines, with particular emphasis on quantifying improvements in both resolution and sensitivity. The proposed 128-element architecture achieves a circumferential sampling pitch of 1.37 mm, representing a four-fold increase in circumferential resolution compared with a conventional 32-element PIG. Huygens-based simulations showed that while single small elements provide fine spatial sampling but reduced sensitivity, the application of water-path delay laws restores coherent beam formation, producing 6 dB beamwidths of 6.93° in 4'' pipes and 3.56° in 6'' pipes that are comparable to the 6.38° and 2.67° obtained with a 6 mm reference element. These quantified results demonstrate that the compensated convex phased-array design simultaneously overcomes the traditional trade-off between resolution and sensitivity in small-diameter ultrasonic PIGs.

Two industrial-focused experiments in 4'' and 6'' pipes confirmed these simulated findings. In the 4'' pipe, phased-array compensation improved SNR by 15.34 dB and reduced wall-thickness measurement error by 0.59 mm and measurement

uncertainty by 1.43 mm relative to single-element operation. In the 6" pipe, B-scan imaging demonstrated superior detectability of flat-bottom holes, with the compensated array reliably resolving defects as small as 2 mm diameter that were not consistently visible using either the 6 mm reference element or a single 1.22 mm element. In summary, the 6" B-scan experiments highlight the complementary benefits of convex phased-array compensation: while large single elements provide strong signals and small elements offer fine sampling, the compensated array achieves both simultaneously, delivering the sensitivity required for practical inline inspection. Together, these results demonstrate the feasibility of convex phased-array beamforming for high-fidelity inspection in small-diameter pipelines.

While these results demonstrate the feasibility of convex phased-array inspection in small-diameter pipelines, there are several limitations. The defects examined were machined flat-bottom holes, which do not fully capture the irregular morphologies encountered in service. In addition, the experimental validation was conducted using a laboratory off-the-shelf phased-array controller. While this provided precise control over excitation, phasing, and data acquisition, it does not reflect the constraints of an embedded, low-power system suitable for inline inspection.

The demonstrated performance suggests strong potential for practical application in oil, gas, and process-industry pipelines, particularly in small-diameter lines that contain tight bends, valves, and geometrical restrictions where existing PIGs perform poorly. Building on this foundation, future work will advance the prototype toward a real-life, deployable inline inspection instrument. A key priority is the integration of the phased-array front end with fully embedded, low-power electronics to eliminate dependence on external laboratory controllers and enable autonomous operation over extended pipeline distances. Dynamic flow-loop trials will also be required to assess mechanical robustness, acoustic coupling stability, and real-time data handling under realistic flow, pressure, and turbulence conditions.

Beyond hardware integration, algorithmic enhancements will be explored. Dynamic delay rules, derived from wall echoes or adaptive beamforming and focusing strategies [31], could be applied to refine beam steering in situ, compensating for variable pipe geometries or coupling conditions. In parallel, machine learning and AI-driven classification approaches offer potential for automated defect detection and sizing, enabling the system to handle large volumes of inspection data and improve probability of detection under diverse field conditions.

Finally, large-scale studies in extended pipe networks will be required to establish a statistically robust probability of detection (POD) and sizing accuracy across a wide range of defect morphologies. These steps will translate the demonstrated benefits of convex phased arrays into a field-ready instrument for challenging 4–6" pipeline geometries.

REFERENCES

- [1] M. Coramik and Y. Ege, "Discontinuity inspection in pipelines: A comparison review," *Measurement*, vol. 111, pp. 359–373, 12 2017. [Online]. Available: <http://dx.doi.org/10.1016/j.measurement.2017.07.058>
- [2] C. Oragwu, D. Molyneux, L. Lawal, and S. Ameh, "Overcoming Challenges of Piggings the Unpiggable Pipelines," in *SPE Nigeria Annual International Conference and Exhibition*. SPE, aug 2 2021. [Online]. Available: <http://dx.doi.org/10.2118/207147-MS>
- [3] M. Idroas, M. A. Aziz, Z. Zakaria, and M. Ibrahim, "Imaging of pipeline irregularities using a PIG system based on reflection mode ultrasonic sensors," *International Journal of Oil, Gas and Coal Technology*, vol. 20, no. 2, p. 212, 2019. [Online]. Available: <http://dx.doi.org/10.1504/IJOGCT.2019.097449>
- [4] X. Peng, U. Anyaoha, Z. Liu, and K. Tsukada, "Analysis of Magnetic-Flux Leakage (MFL) Data for Pipeline Corrosion Assessment," *IEEE Transactions on Magnetics*, vol. 56, no. 6, pp. 1–15, 6 2020. [Online]. Available: <http://dx.doi.org/10.1109/TMAG.2020.2981450>
- [5] A. Pople and P. Integrity, "Magnetic flux leakage pigs or ultrasonic pigs? the case for combined intelligent pig inspections," in *6th International conference, pipeline rehabilitation and maintenance*, 2003, pp. 6–10.
- [6] H. Song, L. Yang, G. Liu, G. Tian, D. Ona, Y. Song, and S. Li, "Comparative Analysis of In-line Inspection Equipments and Technologies," *IOP Conference Series: Materials Science and Engineering*, vol. 382, p. 032021, 7 2018. [Online]. Available: <http://dx.doi.org/10.1088/1757-899X/382/3/032021>
- [7] Q. Ma, W. Liang, and P. Zhou, "A Review on Pipeline In-Line Inspection Technologies," *Sensors*, vol. 25, no. 15, p. 4873, aug 7 2025. [Online]. Available: <http://dx.doi.org/10.3390/s25154873>
- [8] H. Zhu, J. Chen, Y. Lin, J. Guo, X. Gao, Y. Chen, Y. Ge, and W. Wang, "In-Line Inspection (ILI) Techniques for Subsea Pipelines: State-of-the-Art," *Journal of Marine Science and Engineering*, vol. 12, no. 3, p. 417, feb 26 2024. [Online]. Available: <http://dx.doi.org/10.3390/jmse12030417>
- [9] R. Qi, D. R. Yntema, and M. Cao, "An Inline Impedance-Based Leakage Detection Method for Nonconducting Buried Water Mains," *IEEE Transactions on Instrumentation and Measurement*, vol. 74, pp. 1–8, 2025. [Online]. Available: <http://dx.doi.org/10.1109/TIM.2025.3548250>
- [10] G. Ru, B. Gao, Q. Tang, S. Jiang, Y. Zhang, F. Luo, and W. L. Woo, "Electromagnetic Coupling Sensing of Pipe In-Line Inspection System," *IEEE Transactions on Instrumentation and Measurement*, vol. 72, pp. 1–15, 2023. [Online]. Available: <http://dx.doi.org/10.1109/TIM.2023.3310083>
- [11] H. Wei, S. Dong, L. Xu, F. Chen, H. Zhang, and X. Li, "Internal inspection method for crack defects in ferromagnetic pipelines under remanent magnetization," *Measurement*, vol. 242, p. 115907, 1 2025. [Online]. Available: <http://dx.doi.org/10.1016/j.measurement.2024.115907>
- [12] W. Jackson, G. Dobie, C. MacLeod, G. West, C. Mineo, and L. McDonald, "Error Analysis and Calibration for a Novel Pipe Profiling Tool," *IEEE Sensors Journal*, vol. 20, no. 7, pp. 3545–3555, apr 1 2020. [Online]. Available: <http://dx.doi.org/10.1109/JSEN.2019.2960939>
- [13] D. Zhang, W. Jackson, G. Dobie, G. West, and C. MacLeod, "Structure-from-motion based image unwrapping and stitching for small bore pipe inspections," *Computers in Industry*, vol. 139, p. 103664, 8 2022. [Online]. Available: <http://dx.doi.org/10.1016/j.compind.2022.103664>
- [14] S. Hosseinzadeh, W. Jackson, D. Zhang, L. McDonald, G. Dobie, G. West, and C. MacLeod, "A Novel Centralization Method for Pipe Image Stitching," *IEEE Sensors Journal*, vol. 21, no. 10, pp. 11 889–11 898, may 15 2021. [Online]. Available: <http://dx.doi.org/10.1109/JSEN.2020.3031637>
- [15] B. O. Parlak and H. A. Yavasoglu, "A Comprehensive Analysis of In-Line Inspection Tools and Technologies for Steel Oil and Gas Pipelines," *Sustainability*, vol. 15, no. 3, p. 2783, feb 3 2023. [Online]. Available: <http://dx.doi.org/10.3390/su15032783>
- [16] N. A. Rodríguez-Olivares, J. V. Cruz-Cruz, A. Gómez-Hernández, R. Hernández-Alvarado, L. Nava-Balanzar, T. Salgado-Jiménez, and J. A. Soto-Cajiga, "Improvement of Ultrasonic Pulse Generator for Automatic Pipeline Inspection," *Sensors*, vol. 18, no. 9, p. 2950, sep 5 2018. [Online]. Available: <http://dx.doi.org/10.3390/s18092950>
- [17] D. Zhang, R. Watson, G. Dobie, C. MacLeod, D. Lines, W. Galbraith, C. Mineo, and G. Pierce, "Evaluation of Coded Excitations for Autonomous Airborne Ultrasonic Inspection," in *2019 IEEE International Ultrasonics Symposium (IUS)*. IEEE, 10 2019, pp. 1–4. [Online]. Available: <http://dx.doi.org/10.1109/ULTSYM.2019.8926048>
- [18] B. W. Drinkwater and P. D. Wilcox, "Ultrasonic arrays for non-destructive evaluation: A review," *NDT & E International*, vol. 39, no. 7, pp. 525–541, 10 2006. [Online]. Available: <http://dx.doi.org/10.1016/j.ndteint.2006.03.006>
- [19] C. Holmes, B. W. Drinkwater, and P. D. Wilcox, "Post-processing of the full matrix of ultrasonic transmit-receive array data for non-destructive evaluation," *NDT & E International*, vol. 38, no. 8, pp. 701–711,

- 12 2005. [Online]. Available: <http://dx.doi.org/10.1016/j.ndteint.2005.04.002>
- [20] S. J. Lim, Y. L. Kim, S. Cho, and I. K. Park, "Ultrasonic Inspection for Welds with Irregular Curvature Geometry Using Flexible Phased Array Probes and Semi-Auto Scanners: A Feasibility Study," *Applied Sciences*, vol. 12, no. 2, p. 748, Jan 12 2022. [Online]. Available: <http://dx.doi.org/10.3390/app12020748>
- [21] E. Nicolson, E. Mohseni, D. Lines, K. M. Tant, G. Pierce, and C. N. MacLeod, "Towards an in-process ultrasonic phased array inspection method for narrow-gap welds," *NDT & E International*, vol. 144, p. 103074, 6 2024. [Online]. Available: <http://dx.doi.org/10.1016/j.ndteint.2024.103074>
- [22] R. Hampson, D. Zhang, A. Gachagan, and G. Dobie, "Modelling and characterisation ultrasonic phased array transducers for pipe inspections," *International Journal of Pressure Vessels and Piping*, vol. 200, p. 104808, 12 2022. [Online]. Available: <http://dx.doi.org/10.1016/j.ijpvp.2022.104808>
- [23] J. Deng, Y. Zhang, Y. Qu, C. Pei, T. Liu, and Z. Chen, "Development of a flexible phased array electromagnetic acoustic testing system with array pickups," *NDT & E International*, vol. 149, p. 103263, 1 2025. [Online]. Available: <http://dx.doi.org/10.1016/j.ndteint.2024.103263>
- [24] Olympus, "Cobra weld inspection industrial scanner (kit u8750053)." [Online]. Available: <https://ims.evidentscientific.com/en/products/industrial-scanners/U8750053>
- [25] E. Kühnicke, "Curved arrays for pipe wall inspection – fundamentals of electronic focusing for curved and plane arrays," *Wave Motion*, vol. 46, no. 4, pp. 221–236, 2009. [Online]. Available: <https://doi.org/10.1016/j.wavemoti.2009.01.001>
- [26] Z. Qi, M. Liao, L. Sheng, Z. Chen, and Y. Niu, "Circular Phased Array Ultrasonic Transducer Design for Internal Inspection of Natural Gas Pipeline," in *2024 3rd Conference on Fully Actuated System Theory and Applications (FASTA)*. IEEE, May 10 2024, pp. 1299–1304. [Online]. Available: <http://dx.doi.org/10.1109/FASTA61401.2024.10595203>
- [27] J. Jensen, "Simulation of advanced ultrasound systems using Field II," in *2004 2nd IEEE International Symposium on Biomedical Imaging: Macro to Nano (IEEE Cat No. 04EX821)*, vol. 2. IEEE, pp. 636–639. [Online]. Available: <http://dx.doi.org/10.1109/ISBI.2004.1398618>
- [28] Y. Kagawa, T. Tsuchiya, B. Fujii, and K. Fujioka, "Discrete HUYGENS' MODEL APPROACH TO SOUND WAVE PROPAGATION," *Journal of Sound and Vibration*, vol. 218, no. 3, pp. 419–444, 12 1998. [Online]. Available: <http://dx.doi.org/10.1006/jsvi.1998.1861>
- [29] Evident Scientific, "Flexible ultrasonic phased-array probe for complex shape inspection," 2025, accessed: 2025-11-28. [Online]. Available: <https://ims.evidentscientific.com/en/applications/flexible-ultrasonic-phased-array-probe-for-complex-shape-inspection>
- [30] Eddyfi Technologies, "Phased array probes and wedges," 2025, accessed: 2025-11-28. [Online]. Available: <https://www.eddyfi.com/en/product/phased-array-pa-probes-wedges>
- [31] M. Fan, Z. Xie, L. Xu, and J. Ma, "Adaptive Beamforming and Multiwave Fusion for Precise Laser Ultrasound-Based Nondestructive Evaluation," *IEEE Transactions on Instrumentation and Measurement*, vol. 74, pp. 1–9, 2025. [Online]. Available: <http://dx.doi.org/10.1109/TIM.2024.3500048>